Atmos. Chem. Phys. Discuss., 13, 31891–31932, 2013
www.atmos-chem-phys-discuss.net/13/31891/2013/
doi:10.5194/acpd-13-31891-2013

Atmospheric Chemistry and Physics Discussions

High-resolution large-eddy simulations of sub-kilometer-scale turbulence in the upper troposphere lower stratosphere

R. Paoli[1], **O. Thouron**[1], **J. Escobar**[2], **J. Picot**[1], **and D. Cariolle**[1,3]

[1]CNRS/CERFACS, URA1875, Sciences de l'Univers au CERFACS, Toulouse, France
[2]Laboratoire d'Aérologie, Université de Toulouse and CNRS, Toulouse, France
[3]Météo France, Toulouse, France

Received: 16 October 2013 – Accepted: 22 November 2013 – Published: 6 December 2013

Correspondence to: R. Paoli (paoli@cerfacs.fr)

Published by Copernicus Publications on behalf of the European Geosciences Union.

Abstract

Large-eddy simulations of sub-kilometer-scale turbulence in the upper troposphere lower stratosphere (UTLS) are carried out and analyzed using the mesoscale atmospheric model Méso-NH. Different levels of turbulence are generated using a large-scale stochastic forcing technique that was especially devised to treat atmospheric stratified flows. The study focuses on the analysis of turbulence statistics, including mean quantities and energy spectra, as well as on a detailed description of flow topology. The impact of resolution is also discussed by decreasing the grid spacing to 2 m and increasing the number of grid points to 8×10^9. Because of atmospheric stratification, turbulence is substantially anisotropic, and large elongated structures form in the horizontal directions, in accordance with theoretical analysis and spectral direct numerical simulations of stably stratified flows. It is also found that the inertial range of horizontal kinetic energy spectrum, generally observed at scales larger than a few kilometers, is prolonged into the sub-kilometric range, down to the Ozmidov scales that obey isotropic Kolmorogov turbulence. The results are in line with observational analysis based on in situ measurements from existing campaigns.

1 Introduction

The environmental impact of aviation is a problem of increasing concern among scientists and policymakers as commercial air traffic continues to grow (Penner et al., 1999; Lee et al., 2009). Because of long residence time, low background concentrations and large radiative sensitivity at cruise altitude aircraft emissions can influence the chemical and physical state of the atmosphere and affect the radiative budget of the Earth. According to recent evaluations, the induced cloudiness produced by aircraft emissions in the form of contrails and induced cirrus is among the most uncertain contributors to the global radiative forcing (Sausen et al., 2005; Lee et al., 2009). One important reason for this uncertainty is that, although aircraft emissions are (generally) known

ACPD
13, 31891–31932, 2013

at the nozzle exit, their impact depends on their interactions with the atmosphere and should be evaluated at the scales resolved by general circulation models or chemistry transport models, i.e. 100 km or more for grids that cover the entire globe. Predicting the evolution of emissions during all their lifetime is then a crucial step to evaluate their environmental impact and to produce parameterizations for large-scale models. This requires the use of atmospheric models to represent the small-scale motions and the physico-chemical processes occurring in the free atmosphere. In particular, the dispersion of aircraft plumes and the mixing of exhausts with ambient air depend on the properties of atmospheric turbulence in the upper troposphere lower stratosphere (UTLS) where most of flight time is spent during cruise (Gerz et al., 1998).

Understanding and predicting the characteristics of atmospheric turbulence in the UTLS is of paramount importance for aviation (Sharman et al., 2012). Unlike convective turbulence, which is a marker of extreme weather conditions like thunderstorms, intense up- and downdrafts or lighting, turbulence in the UTLS is often associated to less spectacular though less predictable events. For example, clear-air turbulence can be triggered by wind shear, mountain waves or the jet stream, and as such it has been also investigated in the context of aviation safety and hazard (Mecikalski et al., 2007). Because of the scattered and intermittent character of these phenomena it is difficult to reproduce exactly the effect of turbulence resulting from a specific event on a specific aircraft plume. The usual approach employed in the literature has been to represent the general properties of atmospheric turbulence rather than a particular atmospheric situation. For example, in early studies of atmospheric dispersion, aircraft plumes were represented by Gaussian plumes and turbulence was initialized using idealized flow-fields satisfying a given model spectrum (Dürbeck and Gerz, 1995, 1996; Gerz et al., 1998). This procedures may impose a limitation on the duration of the simulation since turbulence is not sustained and eventually decays. By contrast, the objective of the present study is to reproduce and analyze the statistical properties of turbulence by modeling the mechanism of turbulence generation via a suitable large-scale forcing rather than the turbulent flow itself or the initial conditions.

ACPD
13, 31891–31932, 2013

The statistical properties of turbulence in the UTLS were first studied in the seminal paper by Nastrom and Gage (1985) who analyzed observational data from instrumented commercial aircraft during the GASP (Global Atmospheric Sampling Program) campaign. They observed the kinetic energy horizontal spectra vary with wave number k as $k^{-5/3}$ for scales of a few kilometers to a few hundred kilometers, and as k^{-3} for larger scales. Similar results were obtained by Lindborg (1999) who analyzed data from the MOZAIC (Measurements of Ozone Water Vapor by Airbus Aircraft) campaign. This trend has been reproduced since then by means of Direct Numerical Simulations (DNS) and Large-eddy simulations (LES) of ideal turbulent stratified flows that have characteristics similar to those encountered in the UTLS (Métais and Lesieur, 1992; Kaltenbach et al., 1994; Riley and Lelong, 2000; Riley and de Bruyn Kops, 2003; Waite and Bartello, 2004; Lindborg, 2006; Brethouwer et al., 2007; Riley and Lindborg, 2008). The picture emerging from these studies is that an inertial range exists in the horizontal energy spectrum, which is an indication of a downscale transfer of energy from large to small eddies as in classical Kolmogorov turbulence. However, because of atmospheric stratification, turbulence differs from isotropic turbulence, which reflects for example in the presence of large elongated horizontal flow structures. Indeed, the competition between turbulence and stable stratification that tend to compress eddies vertically is the clue that makes the simulation of strongly stratified flows challenging as turbulence can be three-dimensional yet substantially anistropic (Waite and Bartello, 2004; Lindborg, 2006; Brethouwer et al., 2007; Waite, 2011; Kimura and Herring, 2012). The intermediate range of scales between a few kilometers down to a few tens of meters of Ozmidov scale where turbulence can be considered isotropic, is more difficult to observe and to predict numerically because of the high resolutions required to capture the small scale dynamics. While some recent measurements (Wroblewski et al., 2010) seem to support a prolongation of the $k^{-5/3}$ slope, no definitive answer has been found so far to elucidate the characteristics of this range of the spectrum. This is particularly important for the dispersion of aircraft emissions because the transition from the aircraft

ACPD
13, 31891–31932, 2013

wake-controlled to the atmosphere-controlled dynamics occurs exactly at these scales (Dürbeck and Gerz, 1996; Paugam et al., 2010).

The vast majority of DNS and LES studies of stably stratified turbulence reported in the literature were based on non-dimensional spectral formulations of Navier-Stokes equations under the Boussinesq approximation. While this allows for a fine description of turbulent structures and statistics against which mesoscale models can be validated, the inclusion of atmospheric processes like microphysics or radiation can be more problematic in these formulations. In the present work, the properties of turbulence in the UTLS at the sub-kilometer scale are analyzed using a mesoscale atmospheric model that is formulated in physical space. To that end, a method for large-scale turbulence forcing is presented and large-eddy simulations are performed in an idealized atmosphere using computational grids with up to 2 m resolution and up to 2048^3 grid points, one of the largest LES attempted in this area to the authors' knowledge. The choices of the model and the range of scales are motivated by the necessity of dealing with a model that contains all the physics (microphysics, radiative transfer, etc.) needed for studying environmental problems that are relevant to aviation and that will be addressed in follow-up studies. The generation of background turbulence is a first step of a more ambitious project that consists in simulating the evolution of contrails in the free atmosphere and their transition into cirrus clouds. The present paper is organized as follows. Section 2 describes the governing the equations of the model, with emphasis on the forcing methodology used to force turbulence at larger scales. The results of the simulations are discussed in Sect. 3 including the flow statistics, flow topology and energy spectra for different levels of atmospheric turbulence, and some elements of comparison with observational analysis. Conclusions are drawn in Sect. 4.

2 Governing equations and numerical model

The simulations were carried out using Meso-NH, the atmospheric research model developed by Météo France and the Laboratoire d'Aérologie. The model is built around

ACPD
13, 31891–31932, 2013

a dynamical core that is capable to simulate atmospheric motions ranging from the meso-alpha scales down to the micrometer scales; an ensemble of packages treating different physical processes in the atmosphere; a flexible file manager, and an ensemble of pre-processing tools to set up the initial conditions, either idealized or interpolated from meteorological analysis or forecasts (for details, see the online scientific documentation: http://mesonh.aero.obs-mip.fr/mesonh). Briefly, the model solves Navier-Stokes equations in the anelastic approximation (Lipps and Hemler, 1982). The "reference" thermodynamic state is a function of the altitude (the vertical coordinate z). The basic prognostic variables are momentum $\boldsymbol{u} = [u, v, w]$ and potential temperature $\theta = T/\Pi$ where T denotes temperature and $\Pi \equiv (p_{00}/p)^{R_d/c_{p_d}}$ the Exner function where p and p_{00} are the local and ground level pressure, while R_d and c_{p_d} are the gas constant and specific heat of dry air, respectively (Lafore et al., 1998). Additional prognostic variables include mixing ratios of chemical species and water substances limited to water vapor mixing ratio r_v in this study. The virtual potential temperature is then defined as $\theta_v = \theta\left(\frac{R_d + r_v R_v}{R_d + r_v R_d}\right)$ where R_v is the gas constant of water vapor. Coriolis forces are not important at the scales of interest for this study. Phase changes and microphysical processes are not activated. In the LES approach, each variable ϕ is decomposed into a resolved or filtered part $\overline{\phi}$ and a unresolved or subgrid-scale part ϕ' with $\phi \equiv \overline{\phi} + \phi'$. This procedure can be obtained by a convolution integral of the variable with filter functions that depend on filter widths. In the present LES formulation, the filter widths correspond to the grid spacings $\Delta x, \Delta y, \Delta z$, so that filtering is equivalent to grid-averaging. With these hypotheses and neglecting third-order turbulent fluxes, the governing equations read (Lafore et al., 1998; Cuxart et al., 2000):

ACPD
13, 31891–31932, 2013

$$\nabla \cdot (\rho_0 \overline{\boldsymbol{u}}) = 0 \tag{1}$$

$$\frac{\partial(\rho_0 \overline{\boldsymbol{u}})}{\partial t} + \nabla \cdot (\rho_0 \overline{\boldsymbol{u}} \otimes \overline{\boldsymbol{u}}) = \rho_0 \frac{\overline{\theta}_\mathrm{v} - \theta_{\mathrm{v}_0}}{\theta_{\mathrm{v}_0}} \boldsymbol{g} + \rho_0 \overline{\boldsymbol{F}}_\Pi + \rho_0 \overline{\boldsymbol{f}} - \nabla \cdot (\rho_0 \overline{\boldsymbol{u}' \otimes \boldsymbol{u}'}) \tag{2}$$

$$\frac{\partial(\rho_0 \overline{\theta})}{\partial t} + \nabla \cdot (\rho_0 \overline{\boldsymbol{u}}\, \overline{\theta}) = \rho_0 \overline{G_\Pi} - \nabla \cdot (\rho_0 \overline{\boldsymbol{u}' \theta'}) \tag{3}$$

$$\frac{\partial(\rho_0 \overline{r}_\mathrm{v})}{\partial t} + \nabla \cdot (\rho_0 \overline{\boldsymbol{u}}\, \overline{r}_\mathrm{v}) = -\nabla \cdot (\rho_0 \overline{\boldsymbol{u}' r'_\mathrm{v}}) \tag{4}$$

where subscript 0 denotes the reference state; $\boldsymbol{g}$ is the acceleration due to gravity, $\boldsymbol{F}_\Pi = \nabla \left(c_{p_\mathrm{d}} \theta_{\mathrm{v}_0} \left(\overline{\Pi} - \Pi_0 \right) \right)$ is the (filtered) modified pressure, and $G_\Pi = \left(\frac{R_\mathrm{d} + \overline{r}_\mathrm{v} R_\mathrm{v}}{R_\mathrm{d}} \frac{c_{p_\mathrm{d}}}{c_{p_\mathrm{h}}} - 1 \right) \frac{\overline{w}\,\overline{\theta}}{\Pi_0} \frac{\mathrm{d}\Pi_0}{\mathrm{d}z}$ with $c_{p_\mathrm{h}} = c_{p_\mathrm{d}} + \overline{r}_\mathrm{v} c_{p_\mathrm{v}}$ the specific heat of moist air. The term $\overline{\boldsymbol{f}}$ denotes a generic body force, which corresponds to the stochastic forcing in this study and is discussed in the next section. All Reynolds stresses $\overline{\boldsymbol{u}' \otimes \boldsymbol{u}'}$, turbulent fluxes $\overline{\boldsymbol{u}' \theta'}$, $\overline{\boldsymbol{u}' r'_\mathrm{v}}$, and unresolved correlations $\overline{r'_\mathrm{v} \theta'}$, $\overline{\theta'^2}$, are modeled using a closure based on mixing length $L = (\Delta x \Delta y \Delta z)^{1/3}$ (Deardorff, 1972; Redelsperger and Sommeria, 1981) and a prognostic equation for the turbulent kinetic energy, which represents the isotropic part of Reynolds stress tensor,

$$e_\mathrm{t} = \frac{1}{2} \mathrm{tr}(\overline{\boldsymbol{u}' \otimes \boldsymbol{u}'}) \equiv \frac{1}{2} \overline{\boldsymbol{u}' \cdot \boldsymbol{u}'} \tag{5}$$

as explained by Cuxart et al. (2000):

$$\frac{\partial(\rho_0 e_\mathrm{t})}{\partial t} + \nabla \cdot (\rho_0 \overline{\boldsymbol{u}}\, e_\mathrm{t}) = \rho_0 \boldsymbol{g} \cdot \frac{\overline{\boldsymbol{u}' \theta'_\mathrm{v}}}{\theta_{\mathrm{v}_0}} - \rho_0 \overline{\boldsymbol{u}' \otimes \boldsymbol{u}'} \cdot \nabla \overline{\boldsymbol{u}}$$
$$+ \nabla \cdot (C_2 \rho_0 L e_\mathrm{t}^{1/2} \nabla e_\mathrm{t}) - \rho_0 C_\epsilon \frac{e_\mathrm{t}^{3/2}}{L} \tag{6}$$

ACPD
13, 31891–31932, 2013

where $C_2 = 0.2$ and $C_\epsilon = 0.7$ are model constants and the last term in the rhs of Eq. (6) corresponds the turbulent dissipation rate,

$$\epsilon = C_\epsilon \frac{e_t^{3/2}}{L}. \quad (7)$$

Note that the present formulation of the model does not account for the contribution of molecular viscosity to the shear stress tensor. This is justified for atmospheric high Reynolds numbers if the cut-off length (proportional to the grid size) is much larger than the Kolmogrov dissipative scale $\eta \sim (\nu^3/\epsilon)^{1/4}$. For air molecular viscosity $\nu \sim 10^{-5}\,\mathrm{m^2\,s^{-1}}$ and turbulence dissipation rates at the tropopause $\epsilon \sim 10^{-6}$–$10^{-5}\,\mathrm{m^2\,s^{-3}}$ (Lindborg, 1999), the Kolmogorv scale $\eta \sim 10^{-3}\,\mathrm{m}$, which is much smaller than the grid sizes employed in this study.

2.1 Turbulence forcing

In order to obtain a statistically stationary velocity field, a low wave number body force is applied to the momentum equations using the method originally developed by Eswaran and Pope (1988) in spectral space and reformulated by Paoli and Shariff (2009) in physical space. In this method, all modes with wave numbers within a sphere of radius k_f are forced using stochastic processes that mimic the turbulence production at scales larger than the computational domain and allow the nonlinear cascade to determine fluctuations at smaller scales. Denoting by $\Re\{\cdot\}$ and $\Im\{\cdot\}$ the real and imaginary part of a complex number, the body force is represented as a finite Fourier series,

$$\bar{\boldsymbol{f}}(\boldsymbol{x},t) = \sum_{|\boldsymbol{k}|\le k_f} \Re\left\{ e^{\mathrm{i}\boldsymbol{k}\cdot\boldsymbol{x}}\, \hat{\boldsymbol{f}}(\boldsymbol{k},t) \right\} \quad (8)$$

ACPD
13, 31891–31932, 2013

where $i = \sqrt{-1}$, $\boldsymbol{k}$ is the three-dimensional wave number, and $\hat{\boldsymbol{f}}(\boldsymbol{k},t)$ is the amplitude of the complex Fourier mode, which is obtained from the divergence-free projection

$$\hat{\boldsymbol{f}}(\boldsymbol{k},t) = \hat{\boldsymbol{g}}(\boldsymbol{k},t) - \frac{\boldsymbol{k}\cdot\hat{\boldsymbol{g}}(\boldsymbol{k},t)}{|\boldsymbol{k}|^2}\,\boldsymbol{k} \tag{9}$$

of the complex vector $\hat{\boldsymbol{g}}(\boldsymbol{k},t) \equiv \Re\{\hat{\boldsymbol{g}}(\boldsymbol{k},t)\} + \mathrm{i}\,\Im\{\hat{\boldsymbol{g}}(\boldsymbol{k},t)\}$. The latter is composed of six independent Uhlenbeck-Ornstein processes corresponding to the real and imaginary parts of $\hat{\boldsymbol{g}}(\boldsymbol{k},t)$:

$$\mathrm{d}\,\Re\{\hat{\boldsymbol{g}}(\boldsymbol{k},t)\} = -\frac{\Re\{\hat{\boldsymbol{g}}(\boldsymbol{k},t)\}}{\tau_\mathrm{f}}\,\mathrm{d}t + \sigma_\mathrm{f}\sqrt{\frac{2\,\mathrm{d}t}{\tau_\mathrm{f}}}\,\mathcal{N}\big|_t^{t+\mathrm{d}t} \tag{10}$$

$$\mathrm{d}\,\Im\{\hat{\boldsymbol{g}}(\boldsymbol{k},t)\} = -\frac{\Im\{\hat{\boldsymbol{g}}(\boldsymbol{k},t)\}}{\tau_\mathrm{f}}\,\mathrm{d}t + \sigma_\mathrm{f}\sqrt{\frac{2\,\mathrm{d}t}{\tau_\mathrm{f}}}\,\mathcal{M}\big|_t^{t+\mathrm{d}t} \tag{11}$$

where τ_f and σ_f are, respectively, the autocorrelation time and the standard deviation of the process, while $\mathcal{N}\big|_t^{t+\mathrm{d}t}$ and $\mathcal{M}\big|_t^{t+\mathrm{d}t}$ are vector-valued normally distributed random processes with zero mean and unit variance over the time interval $[t, t+\mathrm{d}t]$. The mode corresponding to $\boldsymbol{k} = 0$ is not forced, so from Eq. (8) the net force acting on the flow is zero and no mean motion is created. Furthermore, in the present implementation of the method, the vertical component of the forcing is set to zero. This implies that vertical motions can be attributed to the nonlinear interactions between horizontal and vertical momentum rather than to the direct effect of forcing.

2.2 Numerics

For the momentum components, the spatial discretization relies on a fourth-order finite differences staggered scheme, while time discretization is based on a leapfrog scheme, except for the stochastic body force that is advanced in time using a first order Euler scheme. The piecewise parabolic method (PPM) (Colella and Woodward,

ACPD
13, 31891–31932, 2013

1984) advection scheme is used for all scalar variables. Pressure is obtained by solving a Poisson equation that enforces the divergence-free condition Eq. (1) by means of a FFT algorithm, which was specially devised for treating domain decomposition in massively parallel architectures. The code uses MPI as the basic network communication protocol and has proven good scalability on up to 100 000 parallel cores during various benchmark tests of extreme-scale computing in Europe and in the US (Pantillon et al., 2011). For this study, the simulations were run on 4096 cores of a BullX supercomputer for an overall cost of 7 millions CPU hours.

3 Results

3.1 Computational details

The computational domain is a cubic box with side lengths $\mathcal{L} = 4\,\mathrm{km}$, representing a portion of an idealized atmosphere (see Fig. 1). The reference altitude is 11 km, which is typical of long-haul flights operated by commercial airlines. Values of temperature, pressure and density at this altitude are set to $T_\infty = 218\,\mathrm{K}$, $\rho_\infty = 0.388\,\mathrm{kg\,m^{-3}}$, and $p_\infty = 24\,286\,\mathrm{Pa}$, respectively, and the corresponding potential temperature is $\theta_\infty = 300\,\mathrm{K}$. The background atmospheric fields $\rho_0(z)$ and $\theta_0(z)$ are obtained from the hydrostatic and thermodynamic relations with the Brunt Väisälä frequency set to

$$N = \sqrt{\frac{g}{\theta_0}\frac{\mathrm{d}\theta_0}{\mathrm{d}z}} = 0.012\,\mathrm{s^{-1}}. \tag{12}$$

The background vapor mixing ratio is obtained from climatology of a mid-latitude summer standard atmosphere (Clatchey et al., 1972) with $r_{v_\infty} = 0.001$. The flow is initially at rest, and the spectral shell of the forcing (highest forced wave number) is $k_f = 2\sqrt{2}\,k_0$ where

ACPD
13, 31891–31932, 2013

$$k_0 = \frac{2\pi}{\mathcal{L}} \tag{13}$$

is the fundamental wave number. Periodic boundary conditions are imposed in the horizontal directions x and y, whereas open boundary conditions are used in the vertical direction z in combination with two buffer zones of size $\delta = 200\,\mathrm{m}$ at the top and bottom of the computational domain where the velocity is smoothed down to zero. This boundary condition indirectly leads to the periodicity of velocity and temperature fluctuations in the z direction. However, data in the buffer zones are excluded from post-processing analysis.

3.2 Flow statistics

In order to characterize the flow statistics, the volume average $\langle\phi\rangle$ of a generic quantity ϕ is defined as

$$\langle\phi\rangle(t) = \frac{1}{L_x L_y L_z} \int_0^{L_x}\int_0^{L_y}\int_0^{L_z} \phi(x,y,z,t)\,\mathrm{d}x\,\mathrm{d}y\,\mathrm{d}z \tag{14}$$

where $L_x = L_y = \mathcal{L}$ and $L_z = \mathcal{L} - 2\delta$. The horizontal average $\langle\phi\rangle_\mathrm{h}$ is defined in a similarly way as

$$\langle\phi\rangle_\mathrm{h}(z,t) = \frac{1}{L_x L_y} \int_0^{L_x}\int_0^{L_y} \phi(x,y,z,t)\,\mathrm{d}x\,\mathrm{d}y\,. \tag{15}$$

In the following analysis, the explicit dependence of $\langle\phi\rangle$ and $\langle\phi\rangle_\mathrm{h}$ on t and z will be been omitted for notational ease.

ACPD
13, 31891–31932, 2013

Setting $\phi = \overline{\boldsymbol{u}}$ in Eq. (14) and observing that the flow is initially at rest and the forcing produces zero net acceleration of the flow, yields

$$\langle \overline{\boldsymbol{u}} \rangle = \frac{1}{L_x L_y L_z} \int_0^{L_x} \int_0^{L_y} \int_0^{L_z} \overline{\boldsymbol{u}} \, \mathrm{d}x \, \mathrm{d}y \, \mathrm{d}z = 0 \tag{16}$$

while setting $\phi = \overline{\boldsymbol{u} \otimes \boldsymbol{u}}$ yields

$$\langle \overline{\boldsymbol{u} \otimes \boldsymbol{u}} \rangle = \frac{1}{L_x L_y L_z} \int_0^{L_x} \int_0^{L_y} \int_0^{L_z} \overline{\boldsymbol{u} \otimes \boldsymbol{u}} \, \mathrm{d}x \, \mathrm{d}y \, \mathrm{d}z = \\ = \langle \overline{\boldsymbol{u}} \otimes \overline{\boldsymbol{u}} \rangle + \langle \overline{\boldsymbol{u}' \otimes \boldsymbol{u}'} \rangle \tag{17}$$

where the last two terms of Eq. (17) represent, respectively, the resolved and subgrid-scale contributions to the second order moment of the velocity field. Setting $\phi = e_t$ and using Eq. (5) yields the volume average of the subgrid-scale turbulent kinetic energy,

$$\langle e_t \rangle = \frac{1}{L_x L_y L_z} \int_0^{L_x} \int_0^{L_y} \int_0^{L_z} e_t \, \mathrm{d}x \, \mathrm{d}y \, \mathrm{d}z = \frac{\mathrm{tr} \langle \overline{\boldsymbol{u}' \otimes \boldsymbol{u}'} \rangle}{2} \tag{18}$$

while setting $\phi = E \equiv \frac{\overline{\boldsymbol{u} \cdot \boldsymbol{u}}}{2}$ and using Eqs. (17)–(18) gives

$$\langle E \rangle = \frac{1}{L_x L_y L_z} \int_0^{L_x} \int_0^{L_y} \int_0^{L_z} E \, \mathrm{d}x \, \mathrm{d}y \, \mathrm{d}z = \frac{\langle \overline{\boldsymbol{u}} \cdot \overline{\boldsymbol{u}} \rangle}{2} + \langle e_t \rangle \tag{19}$$

which represents the total mean kinetic energy of the flow. In strongly stratified flows where large anisotropy exists between horizontal and vertical directions, the resolved

ACPD
13, 31891–31932, 2013

velocity $\overline{\boldsymbol{u}}$ can be further decomposed using Eq. (15) into a horizontal mean:

$$\langle \overline{\boldsymbol{u}} \rangle_{\mathrm{h}} \equiv \frac{1}{L_x L_y} \int_0^{L_x} \int_0^{L_y} \overline{\boldsymbol{u}} \, \mathrm{d}x \, \mathrm{d}y \tag{20}$$

and a perturbation with respect to this mean:

$$\overline{\boldsymbol{u}}_{\mathrm{t}} \equiv \overline{\boldsymbol{u}} - \langle \overline{\boldsymbol{u}} \rangle_{\mathrm{h}} \tag{21}$$

with $\langle \overline{\boldsymbol{u}} \rangle_{\mathrm{h}}$ and $\overline{\boldsymbol{u}}_{\mathrm{t}}$ satisfying the identity $\langle \overline{\boldsymbol{u}}_{\mathrm{t}} \rangle \equiv \langle \overline{\boldsymbol{u}} - \langle \overline{\boldsymbol{u}} \rangle_{\mathrm{h}} \rangle = \langle \overline{\boldsymbol{u}} \rangle - \langle \overline{\boldsymbol{u}} \rangle = 0$. Setting $\phi = E_{\mathrm{t}} \equiv \frac{\overline{\boldsymbol{u}}_{\mathrm{t}} \cdot \overline{\boldsymbol{u}}_{\mathrm{t}}}{2}$ in Eq. (14) gives

$$\langle E_{\mathrm{t}} \rangle = \frac{1}{L_x L_y L_z} \int_0^{L_x} \int_0^{L_y} \int_0^{L_z} E_{\mathrm{t}} \, \mathrm{d}x \, \mathrm{d}y \, \mathrm{d}z = \frac{\langle \overline{\boldsymbol{u}}_{\mathrm{t}} \cdot \overline{\boldsymbol{u}}_{\mathrm{t}} \rangle}{2} \tag{22}$$

which represents the mean kinetic energy associated to $\overline{\boldsymbol{u}}_{\mathrm{t}}$. It is interesting to observe that applying the volume average operator to $\overline{\boldsymbol{u}}_{\mathrm{t}} \cdot \overline{\boldsymbol{u}}_{\mathrm{t}}$ and using Eq. (21) yields

$$\langle \overline{\boldsymbol{u}}_{\mathrm{t}} \cdot \overline{\boldsymbol{u}}_{\mathrm{t}} \rangle = \langle \overline{\boldsymbol{u}} \cdot \overline{\boldsymbol{u}} \rangle - \frac{1}{L_z} \int_0^{L_z} \langle \overline{\boldsymbol{u}} \rangle_{\mathrm{h}} \cdot \langle \overline{\boldsymbol{u}} \rangle_{\mathrm{h}} \mathrm{d}z \tag{23}$$

which shows that the second order moments of $\overline{\boldsymbol{u}}$ and $\overline{\boldsymbol{u}}_{\mathrm{t}}$ coincide only if the horizontal mean is zero at each vertical level – a condition that is strictly verified for an infinite domain in the horizontal direction. Hence, using $\overline{\boldsymbol{u}}_{\mathrm{t}}$ instead of $\overline{\boldsymbol{u}}$ allows for a more natural interpretation of turbulence statistics that pertain to scales smaller than those that are directly forced. As observed by Chung and Matheou (2012) this decomposition discounts the energy of the larger horizontal modes from the total kinetic energy budget,

ACPD
13, 31891–31932, 2013

and is particularly useful in the present simulations where the forcing produces local distortions of the flow that can be assimilated to nonuniform shear.

Substituting Eq. (23) into Eq. (19) and using Eq. (22), the mean kinetic energy $\langle E \rangle$ can be recast as

$$\langle E \rangle = \langle E_t \rangle + \langle e_t \rangle + \frac{1}{L_z} \int_0^{L_z} \frac{\langle \overline{\boldsymbol{u}} \rangle_h \cdot \langle \overline{\boldsymbol{u}} \rangle_h}{2} \, dz \tag{24}$$

where the first two terms in the rhs represent the kinetic energy of "genuine" fine-scale turbulence, while the last term represents the energy of shear-like motions. Introducing the variances of the velocity components of $\overline{\boldsymbol{u}}_t$,

$$\sigma_u^2 \equiv \langle \overline{u}_t^2 \rangle, \; \sigma_v^2 \equiv \langle \overline{v}_t^2 \rangle, \; \sigma_w^2 \equiv \langle \overline{w}_t^2 \rangle, \tag{25}$$

the resolved turbulent kinetic energy can be recast as

$$\langle E_t \rangle = \frac{\sigma_u^2 + \sigma_v^2 + \sigma_w^2}{2} \tag{26}$$

while the root-mean square of horizontal turbulent fluctuations is defined by

$$U = \sqrt{\sigma_u^2 + \sigma_v^2} \tag{27}$$

which corresponds to the large-scale (horizontal) vortices (Waite, 2011).

As for Eq. (20), the horizontal mean of potential temperature is defined as

$$\langle \overline{\theta} \rangle_h \equiv \frac{1}{L_x L_y} \int_0^{L_x} \int_0^{L_y} \overline{\theta} \, dx \, dy \simeq \overline{\theta}_0 \tag{28}$$

ACPD
13, 31891–31932, 2013

where the last relation is due to the smooth (constant) gradient of the background potential temperature, and a perturbation with respect to this mean:

$$\overline{\theta}_t \equiv \overline{\theta} - \langle\overline{\theta}\rangle_h \tag{29}$$

with $\langle\overline{\theta}_t\rangle = \langle\overline{\theta} - \langle\overline{\theta}\rangle_h\rangle = \langle\overline{\theta}\rangle - \langle\overline{\theta}\rangle = 0$.

3.3 Evolution of turbulent statistics

Three levels of turbulence were analyzed and denoted by labels "S", "M" and "W" for strong, moderate and weak turbulence, corresponding to three values of the forcing parameter σ_f in Eqs. (10)–(11). The timescale of forcing is kept fixed and equal to $\tau_f = 33.6$ s. The effects of resolution on turbulence characteristics were also analyzed by varying Δ from 10 m to 2 m, with the corresponding number of grid points varying from 400^3 to 2048^3. The nomenclature used for the different runs and values of the main statistical properties are documented in Table 1. Figure 2 shows the mechanism of turbulence generation through the stochastic forcing method for all the simulated cases. The evolution of the resolved turbulent kinetic energy $\langle E_t\rangle$ is characterized by an initial rapid increase between $0 < t < t_1$ with t_1 of the order of 2 to 3 hours. This is followed by a transient phase, $t_1 < t < t_2$ with t_2 generally lesser than 5 hours, until the energy reaches statistically stationary conditions in the sense that it does not increase or decrease monotonically but oscillates around a steady value. It is interesting to observe that this value increases with the forcing level but is roughly independent on the resolution, which is a posteriori verification that the turbulence model has no or limited impact on the mean resolved quantities. The ratio $\mathcal{R} = \langle e_t\rangle/(\langle E_t\rangle + \langle e_t\rangle)$ of the subgrid-scale to the total turbulent kinetic energy is shown in Fig. 3. As expected, this ratio increases when decreasing the resolution and the turbulence forcing, which reflects the fact that the contribution of the subgrid-scale stress to the total Reynolds stress increases. However, in all cases $\mathcal{R} < 0.1$ which meets the classical requirement proposed by Pope (2000) for "well resolved" LES that the resolved turbulent kinetic energy should be at least 80 % of the total energy. The evolution of the mean dissipation

ACPD
13, 31891–31932, 2013

rate is shown in Fig. 4. The initial condition for ϵ corresponds to the threshold value that is initially assigned to the subgrid-scale energy to trigger grid-scale perturbations and initiate the process of energy transfer from the large forced scales to the small dissipative scales. Once the transfer is fully sustained by the forcing, the turbulence model should be able to create its proper dynamics and $\langle e_t \rangle$ should increase, indicating that energy is correctly dissipated at the grid-scale level. This condition is verified for all cases except the lowest resolution for low and moderate turbulence (run W10 where $\langle \epsilon \rangle \simeq \langle \epsilon \rangle(0)$ during all the simulation time), which indicates a slightly inaccurate representation of turbulence at the smallest resolved scales for these cases. This point is further discussed in the next sections. It can be observed that $\langle \epsilon \rangle$ starts to increases at $t \simeq t_1$, corresponding to the effective activation of the turbulence model, and then attains a statistically steady value. Figure 5 shows the rms of turbulent velocities for the selected case M04. The figure provides a first indication of the anisotropic character of stratified turbulence, with horizontal fluctuations σ_u and σ_v much larger than vertical fluctuations σ_w (the same behavior is observed for all other cases). The anisotropy ratio is $\sigma_u/\sigma_w \simeq 0.3$–$0.4$ depending on the cases and is in the range of available observational data (Nastrom and Gage, 1985).

3.4 Turbulent structures

The turbulent structures of the flow are visualized in Fig. 6 by means of snapshots of potential temperature fluctuations $\overline{\theta}_t$, Eq. (29) at selected vertical (xz) and horizontal (xy) planes for three levels of forcing (runs W10, M10, and S10). The horizontally layered structures ("pancakes") typical of stably stratified flows are visible in xz planes, whereas in the xy planes the dominant structures resemble the large-scale turbulent eddies of classical Kolmogorov turbulence. It is also interesting to observe that, as forcing is increased, the initially thin and patchy layers become thicker and more chaotic, as the consequence of the increase potential of turbulent eddies to overturn against background stratification. These flow characteristics can be quantified by monitoring the evolution of the buoyancy scale,

ACPD
13, 31891–31932, 2013

$$L_b = 2\pi \frac{U}{N} \tag{30}$$

that is reported in Fig. 7 for all the simulated cases (note the factor 2π accounts for the transformation from wave numbers to wavelengths as discussed by Waite and Bartello, 2004; Waite, 2011). The buoyancy scale characterizes the thickness of the shear layers in stratified turbulence (Waite, 2011) and is also associated with the zigzag instability of columnar vortices (Billant and Chomaz, 2000) and overturning of internal gravity waves (Waite and Bartello, 2006). As shown in Fig. 7, L_b varies between 250 m and 300 m depending on the cases, which is well above the grid sizes used for the simulations. This guarantees that the largest vertical structures of the flow are resolved. The ratio $L_b/L_z < 0.1$, which also guarantees that the flow is not vertically confined.

In addition to the buoyancy scale, in LES of stratified turbulence it would be beneficial to resolve the Ozmidov scale,

$$L_O = 2\pi \left(\frac{\epsilon}{N^3}\right)^{1/2} \tag{31}$$

which represents the largest scale turbulent eddies can overturn without being sensibly affected by stratification. As indicated in Table 1, in the strongest forcing case L_O = 35 m, which can be resolved even with the largest grid size Δ = 10 m. For the low and moderate forcing cases, L_O = 15 m and 20 m, respectively, so that, again, the Ozmidov scale can be resolved using Δ = 2 m or Δ = 4 m. On the other hand, with a grid size Δ = 10 m, L_b is (very) barely resolved in the moderate forcing case and is definitely unresolved for the weak forcing case. If the very smallest scales of the flow are not properly resolved, the subgrid-scale model tends to slightly over dissipate at those scales, which affects the kinetic energy spectrum as discussed in Sect. 3.5.

The effects of resolution on the flow can be also appreciated by analyzing the gradient Richardson number, which is a measure of the relative strength between buoyancy

ACPD
13, 31891–31932, 2013

and shear. Denoting by $S^2 \equiv \left(\frac{\partial \bar{u}}{\partial z}\right)^2 + \left(\frac{\partial \bar{v}}{\partial z}\right)^2$ the local vertical shear, one can define the horizontally averaged Richardson number

$$\mathrm{Ri} \equiv \frac{N^2}{\langle S^2 \rangle_\mathrm{h}} \tag{32}$$

where the horizontal average $\langle S^2 \rangle_\mathrm{h}$ is obtained by setting $\phi = s^2$ in Eq. (15). The Richardson number is often associated to the stability of stratified shear flows: for example, it is known from linear stability analysis (Miles, 1961; Howard, 1961) that an initially laminar flow becomes unstable (eventually evolving into a turbulent flow) below the critical value $\mathrm{Ri}_\mathrm{c} = 0.25$; furthermore, values of $\mathrm{Ri} < 1$ have been consistently measured in experimental observations and numerical simulations (Riley and de Bruyn Kops, 2003; Brethouwer et al., 2007). This picture is consistent with the vertical profiles and the probability density function (PDF) of Ri_h that are reported in Fig. 9 and Fig. 8, respectively. As a general trend, the Richardson number decreases when increasing turbulence forcing as this can produce locally stronger shear (Riley and de Bruyn Kops, 2003; Kimura and Herring, 2012). In the high resolution cases, $\Delta = 2\,\mathrm{m}$, Ri_h fluctuates around 0.1 and 0.15 for the weak and moderate forcing, respectively. On the other hand, in the low resolution cases, $\Delta = 10\,\mathrm{m}$, these values fluctuates around $\mathrm{Ri}_\mathrm{h} > 1$ for the weak forcing, $\mathrm{Ri} \lesssim 1$ for the moderate forcing, and $\mathrm{Ri} \simeq 0.5$, well above 1, for the strongest turbulence. This again suggests that with a resolution of $\Delta = 10\,\mathrm{m}$ the strongest turbulence is well resolved, the moderate turbulence is barely resolved and the weak turbulence is not resolved. To further verify this point, we compared the Ri profiles obtained from the 10 m resolution LES data with those obtained by filtering the 2 m resolution data over 5 cells in all directions so that the support of the filtered data is also 10 m. Interestingly, in the moderate turbulence case the profiles of the filtered data and unfiltered data are very similar, which is somehow an a posteriori verification that the cut-off lengths associated to the grid-sizes $\Delta = 2\,\mathrm{m}$ and $\Delta = 10\,\mathrm{m}$ are both situated below the Ozmidov scale in the inertial range of isotropic turbulence. In the weak

ACPD
13, 31891–31932, 2013

turbulence case, the filtered profile are still apart and sensibly lower than the corresponding data from the unfiltered data, as the cut-off length of $\Delta = 10\,\mathrm{m}$ is larger than the Ozmidov scale.

3.5 Energy spectra

Given the discretization of physical space, the (discrete) three-dimensional wave numbers in spectral space are

$$\boldsymbol{k_n} \equiv \boldsymbol{k}_{n_x,n_y,n_z} = [k_{n_x}, k_{n_y}, k_{n_z}] \tag{33}$$

where integers n_x, varying between $1 - N_x/2$ and $N_x/2$, both inclusive, identify modes number in the direction x, while k_x are the corresponding wave numbers:

$$k_{n_x} = \Delta k_x n_x = \frac{2\pi}{L_x} n_x \tag{34}$$

where Δk_x is the wave number spacing. Similar relations hold for y and z directions. The velocity field can be analyzed in spectral space by operating a three-dimensional Fourier transform to the resolved velocity field,

$$\hat{\boldsymbol{u}}(\boldsymbol{k_n}) = \frac{1}{L_x L_y L_z} \int_0^{L_x}\int_0^{L_y}\int_0^{L_z} \overline{\boldsymbol{u}} \exp(-\mathrm{i}\,\boldsymbol{k_n}\cdot\boldsymbol{x})\,\mathrm{d}x\,\mathrm{d}y\,\mathrm{d}z \tag{35}$$

where

$$\hat{\boldsymbol{u}}(\boldsymbol{k_n}) \equiv \hat{\boldsymbol{u}}_{\boldsymbol{n}} = \hat{\boldsymbol{u}}_{n_x,n_y,n_z} \tag{36}$$

are the coefficients of the Fourier modes that can be calculated by applying a FFT algorithm to Eq. (35). Note that in the present approach, periodic boundary conditions

ACPD
13, 31891–31932, 2013

are strictly enforced in the two horizontal directions of the computational domain while in the vertical direction, it is the presence of the top and bottom buffer layers that drives the velocity to zero and implicitly insures the periodicity. The energy of the Fouriers modes are defined as

$$\widehat{E}(\boldsymbol{k_n}) \equiv \widehat{E}_{\boldsymbol{n}} = \widehat{E}_{n_x,n_y,n_z} = \frac{1}{2}\hat{\boldsymbol{u}}_{\boldsymbol{n}} \cdot \hat{\boldsymbol{u}}^*_{\boldsymbol{n}} \tag{37}$$

where the symbol $*$ indicates complex conjugate. The one-dimensional spectra of kinetic energy (density of energy per unit wave number) in each of three coordinate directions are obtained by summing up the energy contribution of all Fourier modes that have the same (absolute) mode number in that direction:

$$\mathcal{E}_x = \frac{1}{\Delta k_x} \sum_{n_y=1-N_y/2}^{N_y/2} \sum_{n_z=1-N_z/2}^{N_z/2} \widehat{E}_{n_x,n_y,n_z} + \widehat{E}_{-n_x,n_y,n_z} \qquad \text{with } n_x = 1,..,N_x/2 \tag{38}$$

$$\mathcal{E}_y = \frac{1}{\Delta k_y} \sum_{n_x=1-N_x/2}^{N_x/2} \sum_{n_z=1-N_z/2}^{N_z/2} \widehat{E}_{n_x,n_y,n_z} + \widehat{E}_{n_x,-n_y,n_z} \qquad \text{with } n_y = 1,..,N_y/2 \tag{39}$$

$$\mathcal{E}_z = \frac{1}{\Delta k_z} \sum_{n_x=1-N_x/2}^{N_x/2} \sum_{n_y=1-N_y/2}^{N_y/2} \widehat{E}_{n_x,n_y,n_z} + \widehat{E}_{n_x,n_y,-n_z} \qquad \text{with } n_z = 1,..,N_z/2 \tag{40}$$

so that for the reality condition, the spectral energy is stored in only half of the modes in each direction. We also define horizontal mode numbers n_h, varying between 1 and $N_\mathrm{h} \equiv N_x = N_y$, and vertical mode numbers n_v, varying between 1 and $N_\mathrm{v} \equiv N_z$. The corresponding horizontal and vertical wave numbers $(k_\mathrm{h}, k_\mathrm{v})$ and wavelengths $(\lambda_\mathrm{h}, \lambda_\mathrm{v})$ are:

ACPD
13, 31891–31932, 2013

$$k_h = \Delta k_h n_h \quad \text{and} \quad \lambda_h = \frac{2\pi}{k_h}, \quad n_h = 1, .., N_h, \tag{41}$$

$$k_v = \Delta k_v n_v \quad \text{and} \quad \lambda_v = \frac{2\pi}{k_v}, \quad n_v = 1, .., N_v. \tag{42}$$

with $\Delta k_h \equiv \Delta k_x = \Delta k_y$ and $\Delta k_v \equiv \Delta k_z$ The horizontal energy spectrum is defined as the average of the one-dimensional energy spectra in the x and y directions while the vertical spectrum is simply the one-dimensional energy spectrum in the z direction (Lindborg, 2006):

$$\mathcal{E}_h = \frac{1}{2}(\mathcal{E}_x + \mathcal{E}_y) \tag{43}$$

$$\mathcal{E}_v = \mathcal{E}_z. \tag{44}$$

Based on dimensional arguments similar to those employed for classical Kolmogorov turbulence, Lindborg (2006) argued that in strongly stratified flows $\mathcal{E}_h$ should scale as $k_h^{-5/3}$ in the inertial range – even though this scaling is associated to the existence of horizontal turbulence cascade rather than to fully developed three-dimensional turbulence. In the inertial range, the theoretical horizontal spectrum then takes the form

$$\mathcal{E}_h^{th} = C_h \langle\epsilon\rangle^{2/3} k_h^{-5/3} \tag{45}$$

where C_h is a constant.

Figure 11 reports the computed horizontal spectra $\mathcal{E}_h$ for all considered cases along with the corresponding spectra compensated using Eq. (45). It can be noticed in the simulations with higher resolutions, $\Delta = 2$ m and 4 m, that the spectra do show an inertial range with $C_h = \mathcal{E}_h / \langle\epsilon\rangle^{2/3} k_h^{-5/3}$ approximately constant in the sub-kilometer scales range, which is of interest to this study, down to the scales of the order of 10 m and below where energy is dissipated by the turbulence model. In particular, in the cases with

ACPD
13, 31891–31932, 2013

highest resolution for the most resolved cases, $C_h \sim 0.4$–0.5, which is of the order of Kolmogorov constant for isotropic turbulence $C_{kol} \simeq 0.49$ (Pope, 2000). The present results are also in line with previous spectral spectral DNS (Lindborg, 2006; Brethouwer et al., 2007; Kimura and Herring, 2012) that considered atmospheric scales larger than those studied here. When the forcing is increased, the portion of the spectrum with $-5/3$ slope tends to increase, which is consistent with the fact that the strength of the turbulence increases relative to the buoyancy force. This tendency can be best appreciated by looking at the compensated spectra of Fig. 11. In the case of weak forcing (and partially for the moderate forcing), when the grid size is decreased to $\Delta = 10\,\mathrm{m}$, the spectra start to depart from the inertial range at scales much larger than the cut-off length of $2\,\Delta$, which is a marker of excessive dissipation produced by the subgrid-scale model. For stratified flows, this is can be explained by the fact that when turbulence is decreased (or stratification is increased) the thickness of vertical layers also reduces so that finer grid resolution is needed to resolve smaller and smaller structures. In particular Waite (2011) showed that the buoyancy scale has to be well resolved both in the horizontal and vertical directions. As for horizontal spectra, it is possible to derive a theoretical expression for the kinetic energy vertical spectra based on dimensional arguments that is valid between buoyancy and the Ozmidov length scales (Billant and Chomaz, 2001; Lindborg, 2006),

$$\mathcal{E}_v^{th} = C_v N^2 k_v^{-3} \tag{46}$$

where C_v is a constant. The vertical spectra $\mathcal{E}_v$ and the compensated spectra $\mathcal{E}_v/N^2 k_v^{-3}$ are plotted in Fig. 12c for all the simulated cases. It can be observed that the scaling is pretty well satisfied in the range of wavelengths $50\,\mathrm{m} < \lambda_v < 200\,\mathrm{m}$.

3.6 Comparison with observations

In this section, some elements of comparison with observational analysis are provided, mainly based on data-sets from the GASP and MOZAIC programs. The focus is laid on

ACPD
13, 31891–31932, 2013

three aspects of validation: the slope of (horizontal) kinetic energy spectra; the value of turbulence dissipation rate $\langle\epsilon\rangle$ and (to a limited extent) the variances of turbulent fluctuations.

Lindborg (1999) computed the longitudinal and transversal structure functions of the velocity field using MOZAIC data and derived a semi–empirical relations that best fit the data. This analysis showed that for separation distances in the range $10^0\,\mathrm{km} \lesssim r \lesssim 10^2\,\mathrm{km}$, the structure functions scale as $r^{2/3}$, which corresponds to the $k_\mathrm{h}^{-5/3}$ scaling of kinetic energy spectra obtained by Nastrom and Gage (1985) using GASP data. Assuming that the spectrum can be extrapolated down to the sub-kilometer scales, this is in good agreement with the spectra shown in Fig. 11. Some existing observations based on individual flights (Wroblewski et al., 2010), in situ measurements with balloons (Dewan, 1997) and radar measurements (Fukao et al., 1994) also support this scaling in the sub-kilometer scales.

The average dissipation rate based on all MOZAIC data was $\langle\epsilon\rangle \sim 6\times10^{-5}\,\mathrm{m^2\,s^{-3}}$ with some minor variations with respect to the latitude (Lindborg, 1999; Lindborg and Cho, 2001). Similar values were reported by Frehlich and Sharman (2010) from detailed climatology analysis of rawinsonde data and by Fukao et al. (1994) based on routine meteorological observations, and were also reproduced by Numerical Weather Prediction models outputs at scales of 50 km and above (Frehlich and Sharman, 2004). All these data seem to support the results shown in Fig. 4 showing that $\langle\epsilon\rangle = \mathcal{O}(10^{-5})\,\mathrm{m^2\,s^{-3}}$. As observed by Lindborg and Cho (2001), these values should not be interpreted as accurate or universal given the intermittent distribution of ϵ in the atmosphere. Indeed, the variance increases when decreasing the averaging length used to calculate from NWP model outputs (Frehlich and Sharman, 2004). Nevertheless, these numbers are useful in that they give an order of magnitude for model comparison.

Finally, the variances of turbulent fluctuations were obtained by Nastrom and Gage (1985) by integrating the energy spectrum for different ranges of wavelengths and averaging for different scenarios (season, latitude, land/see, etc.). As shown, in Table 2, for

ACPD
13, 31891–31932, 2013

wavelengths 12.5 km < λ_h < 25 km they reported U^2 = 0.388 when averaging all flights, which is in the range of values obtained in the present study (even though the scales are slightly above those considered here).

4 Conclusions and perspectives

High-resolution large-eddy simulations of sub-kilometer-scale turbulence in the upper troposphere lower stratosphere were carried out with the atmospheric model Méso-NH on computational meshes of up to 8×10^9 grid points. Turbulence was sustained by means of a low wavenumber stochastic forcing method, which allows the flow to reach statitically steady conditions. Turbulence fluctuations and dissipation rates increase with the forcing. In accordance to previous DNS of stably stratified flows, atmospheric stratification leads to a substantially anisotropy of the flow-field, which manifests with the presence of elongated horizontal structures. The competition between turbulence and stratification controls the degree of the anisotropy, which increases when forcing is reduced. This was quantified in terms of local Richardson number which decreases with the forcing intensity. When forcing is decreased, buoyancy forces tend to overwhelm turbulence, which results in smaller gradients requiring smaller grid size to be resolved. This impacts the slope of the energy spectrum: for low and moderate forcing, the resolution of 2 and 4 m are needed to have a correct inertial range with slope close to $-5/3$ in accordance with theoretical analysis whereas, for strong forcing, 10 m resolution is sufficient. Similar arguments hold for the vertical energy spectrum that has a narrow -3 slope between the buoyancy and Ozimdov scales, in accordance with scaling arguments. Considering the scattered and intermittent nature of turbulence in the UTLS, the present results agree reasonably well with available observational analysis. The slope of energy spectrum, the dissipation rate, and velocity variances are in the range of values obtained from measurements at scales comparable or slightly larger than those considered here. This study demonstrated the capability of atmospheric models to reproduce turbulence in the UTLS in the critical sub-kilometer scale range.

ACPD
13, 31891–31932, 2013

This also opens interesting perspectives for future research, including the activation of atmospheric physicochemical process in the present LES configuration. In particular, the generated turbulence serves as background flow-field in follow-up studies addressing the problem of atmospheric dispersion of aircraft emissions.

Acknowledgements. Financial support from DGAC (Direction Général de l'Aviation Civile) through the project TC2 (Traînés de Condensation et Climat) is gratefully acknowledged. We also acknowledge PRACE (Partnership for Advanced Computing in Europe) research infrastructure for awarding us access to resources through project no. 2011040559 on CURIE supercomputer system located in France at the Très Grand Centre de Calcul (TGCC).

The publication of this article is financed by CNRS-INSU.

References

Billant, P. and Chomaz, J.-M.: Theoretical analysis of the zigzag instability of a vertical columnar vortex pair in a strongly stratified fluid, J. Fluid Mech., 419, 29–63, 2000. 31907

Billant, P. and Chomaz, J.-M.: Self-similarity of strongly stratified inviscid flows, Phys. Fluids, 13, 1645–1651, 2001. 31912

Brethouwer, G., Billant, P., Lindborg, E., and Chomaz, J.-M.: Scaling analysis and simulation of strongly stratified turbulent flows, J. Fluid Mech., 585, 343–368, 2007. 31894, 31908, 31912

Chung, D. and Matheou, G.: Direct numerical simulation of stationary homogeneous stratified sheared turbulence, J. Fluid Mech., 696, 434–467, 2012. 31903

Clatchey, R. A. M., Fenn, R. W., Selby, J. E. A., Volz, F. E., and Garing, J. S.: Optical Properties of the Atmosphere, 3rd edn, Tech. Rep. AFCRL-72-0497, Air Force Cambridge Research Laboratories, 1972. 31900

ACPD
13, 31891–31932, 2013

Colella, P. and Woodward, P. R.: The piecewise parabolic method (PPM) for gas dynamical simulations, J. Comput. Phys., 54, 174–201, 1984. 31899
Cuxart, J., Bougeault, P., and Redelsperger, J.-L.: A turbulence scheme allowing for mesoscale and large scale eddy simulations, Q. J. Roy. Meteor. Soc., 126, 1–30, 2000. 31896, 31897
Deardorff, J. W.: Numerical investigation of neutral and unstable planetary boundary layers, J. Atmos. Sci., 29, 91–115, 1972. 31897
Dewan, E.: Saturated-cascade similitude theory of gravity wave spectra, J. Geophys. Res., 102, 29799–29817, 1997. 31913
Dürbeck, T. and Gerz, T.: Large-eddy simulations of aircraft exhaust plumes in the free atmosphere, effective diffusivities and cross-sections, Geophys. Res. Lett., 22, 3203–3206, 1995. 31893
Dürbeck, T. and Gerz, T.: Dispersion of aircraft exhausts in the free atmosphere, J. Geophys. Res., 101, 26007–26016, 1996. 31893, 31895
Eswaran, V. and Pope, S. B.: An examination of forcing in direct numerical simulations of turbulence, Comput. Fluids, 16, 257–278, 1988. 31898
Frehlich, R. and Sharman, R.: Estimates of turbulence from numerical weather prediction model output with applications to turbulence diagnosis and data assimilation, Mon. Weather Rev., 132, 2308–2324, 2004. 31913
Frehlich, R. and Sharman, R.: Climatology of velocity and temperature turbulence statistics determined from rawinsonde and ACARS/AMDAR Data, J. Appl. Meteor. Climatol., 49, 1149–1169, 2010. 31913, 31920
Fukao, S., Yamanaka, M. D., Ao, N., Hocking, W. K., Sato, T., Yamamoto, M., Nakamura, T., Tsuda, T., and Kato, S.: Seasonal variability of vertical eddy diffusivity in the middle atmosphere 1. Three-year observations by the middle and upper atmosphere radar, J. Geophys. Res., 99, 18973–18987, 1994. 31913, 31920
Gerz, T., Dürbeck, T., and Konopka, P.: Transport and effective diffusion of aircraft emissions, J. Geophys. Res., 103, 25905–25914, 1998. 31893
Howard, L. N.: Note on a paper of John W. Miles, J. Fluid Mech., 10, 509–512, 1961. 31908
Kaltenbach, H.-J., Gerz, T., and Schumann, U.: Large-eddy simulation of homogeneus turbulence and diffusion in stably stratified shear flow, J. Fluid Mech., 280, 1–40, 1994. 31894
Kimura, Y. and Herring, J. R.: Energy spectra of stably stratified turbulence, J. Fluid Mech., 698, 19–50, 2012. 31894, 31908, 31912

ACPD
13, 31891–31932, 2013

Lafore, J. P., Stein, J., Asencio, N., Bougeault, P., Ducrocq, V., Duron, J., Fischer, C., Héreil, P., Mascart, P., Masson, V., Pinty, J. P., Redelsperger, J. L., Richard, E., and Vilà-Guerau de Arellano, J.: The Meso-NH Atmospheric Simulation System. Part I: adiabatic formulation and control simulations, Ann. Geophys., 16, 90–109, doi:10.1007/s00585-997-0090-6, 1998. 31896

Lee, D., Fahey, D. W., Foster, P. M., Newton, P. J., Wit, R. C. N., Lim, L. L., Owen, B., and Sausen, R.: Aviation and the global climate change in the 21th century, Atmos. Environ., 43, 3520–3537, 2009. 31892

Lindborg, E.: Can the atmospheric kinetic energy spectrum be explained by two-dimensional turbulence?, J. Fluid Mech., 388, 259–288, 1999. 31894, 31898, 31913, 31920

Lindborg, E.: The energy cascade in a strongly stratified fluid, J. Fluid Mech., 550, 207–242, 2006. 31894, 31911, 31912

Lindborg, E. and Cho, J. Y. N.: Horizontal velocity structure functions in the upper troposphere and lower stratosphere 2. Theoretical considerations, J. Geophys. Res., 106, 10233–10241, 2001. 31913, 31920

Lipps, F. and Hemler, R. S.: A scale analysis of deep moist convection and some related numerical calculations, J. Atmos. Sci., 39, 2192–2210, 1982. 31896

Mecikalski, J. R., Berendes, T. A., Feltz, W. F., Bedka, K. M., Bedka, S. T., Murray, J. J., Wimmers, A. J., Minnis, P., Johnson, D. B., Haggerty, J., Bernstein, B., Pavolonis, M., and Williams, E.: Aviation applications for satellite-based observations of cloud properties, convection initiation, in-flight icing, turbulence, and volcanic ash, B. Am. Meteorol. Soc., 88, 1589–1607, 2007. 31893

Métais, O. and Lesieur, M.: Spectral large-eddy simulation of isotropic and stably stratified turbulence, J. Fluid Mech., 239, 157–194, 1992. 31894

Miles, J. W.: On the stability of heterogeneous shear flows, J. Fluid Mech., 10, 496–508, 1961. 31908

Nastrom, G. D. and Gage, K. S.: A climatology of atmospheric wave number spectra of wind and temperature observed by commercial aircraft, J. Atmos. Sci., 42, 950–960, 1985. 31894, 31906, 31913, 31920

Pantillon, F., Mascart, P., Chaboureau, J.-P., Lac, C., Escobar, J., and Duron, J.: Seamless MESO-NH modeling over very large grids, C. R. Mecanique, 339, 136–140, 2011. 31900

Paoli, R. and Shariff, K.: Turbulent condensation of droplets: direct simulation and a stochastic model, J. Atmos. Sci., 66, 723–740, 2009. 31898

ACPD
13, 31891–31932, 2013

Paugam, R., Paoli, R., and Cariolle, D.: Influence of vortex dynamics and atmospheric turbulence on the early evolution of a contrail, Atmos. Chem. Phys., 10, 3933–3952, doi:10.5194/acp-10-3933-2010, 2010. 31895

Penner, J. E., Lister, D. H., Griggs, D. J., Dokken, D. J., and McFarland, M., eds.: Aviation and the Global Atmosphere, A special report of IPCC (Intergovernmental Panel on Climate Change), Cambridge University Press, 1999. 31892

Pope, S. B.: Turbulent flows, Cambridge University Press, 2000. 31905, 31912

Redelsperger, J.-L., and Sommeria, G.: Méthode de représentation de la turbulence d'échelle inférieure à la maille pour un modèle tri-dimensionnel de convection nuageuse, Boundary-Layer Meteorol., 21, 509–530, 1981. 31897

Riley, J. J. and de Bruyn Kops, S. M.: Dynamics of turbulence strongly influenced by buoyancy, Phys. Fluids, 15, 2047–2059, 2003. 31894, 31908

Riley, J. J. and Lelong, M.-P.: Fluid motions in the presence of strong stable stratification, Annu. Rev. Fluid Mech., 32, 613–657, 2000. 31894

Riley, J. J. and Lindborg, E.: Stratified turbulence: a possible interpretation of some geophysical turbulence measurements, J. Atmos. Sci., 65, 2416–2424, 2008. 31894

Sausen, R., Isaksen, I., Grewe, V., Lee, D. H. D. S., Myhre, G., Köhler, M. O., Pitari, G., Schumann, U., Stordal, F., and Zerefos, C.: Aviation radiative forcing in 2000: an update on IPCC, Meteorol. Z., 14, 555–561, 2005. 31892

Sharman, R. D., Trier, S. B., Lane, T. P., and Doyle, J. D.: Sources and dynamics of turbulence in the upper troposphere and lower stratosphere: a review, Geophys. Res. Lett., 39, L12803, doi:10.1029/2012GL051996, 2012. 31893

Waite, M. L.: Stratified turbulence at the buoyancy scale, Phys. Fluids, 23, 066602, doi:10.1063/1.3599699, 2011. 31894, 31904, 31907, 31912

Waite, M. L. and Bartello, P.: Stratified turbulence dominated by vortical motion, J. Fluid Mech., 517, 281–308, 2004. 31894, 31907

Waite, M. L. and Bartello, P.: The transition from geostrophic to stratified turbulence, J. Fluid Mech., 568, 89–108, 2006. 31907

Wroblewski, D. E., Coté, O. R., Hacker, J. M., and Dobosy, R. J.: Velocity and temperature structure functions in the upper troposphere and lower stratosphere from high-resolution aircraft measurements, J. Atmos. Sci., 67, 1157–1170, 2010. 31894, 31913, 31920

ACPD
13, 31891–31932, 2013

Table 1. Overview of numerical simulations and principal statistics properties of the flow: run identifier, total number of grid points N_{grid}; resolution Δ; forcing intensity σ_f; turbulent fluctuations $\sigma_u, \sigma_v, \sigma_w$; ratio of subgrid-scale to total turbulent kinetic energy $\langle e_t \rangle / (\langle E_t \rangle + \langle e_t \rangle)$; turbulence dissipation rate $\langle \epsilon \rangle$; buoyancy scale L_b; and Ozmidov scale L_O. For definitions, see Sects. 2.1, 3.2, and 3.4. Data are averaged over the last hour of simulation time during which turbulence is fully sustained by the forcing.

run	N_{grid}	Δ(m)	σ_f(ms^{-2})	σ_u(ms^{-1})	σ_v(ms^{-1})	σ_w(ms^{-1})	$\langle e_t \rangle / (\langle E_t \rangle + \langle e_t \rangle)$	$\langle \epsilon \rangle$(m^2 s^{-3})	L_b(m)	L_O(m)
S10	400^3	10	1.6×10^{-4}	0.498	0.500	0.134	2.08×10^{-2}	5.77×10^{-5}	370	36.2
M10	400^3	10	1.2×10^{-4}	0.382	0.402	0.095	3.13×10^{-2}	5.43×10^{-5}	297	35.2
W10	400^3	10	0.8×10^{-4}	0.323	0.332	0.063	4.40×10^{-2}	5.39×10^{-5}	246	35.1
M04	1024^3	4	1.2×10^{-4}	0.400	0.406	0.117	7.43×10^{-3}	1.64×10^{-5}	300	19.4
W04	1024^3	4	0.8×10^{-4}	0.374	0.342	0.076	6.13×10^{-3}	8.49×10^{-6}	253	13.9
M02	2048^3	2	1.2×10^{-4}	0.445	0.461	0.120	4.93×10^{-3}	1.84×10^{-5}	341	20.5
W02	2048^3	2	0.8×10^{-4}	0.363	0.409	0.084	3.64×10^{-3}	8.14×10^{-6}	303	13.6

ACPD
13, 31891–31932, 2013

Table 2. Comparison with data from observational analysis. Variances from Nastrom and Gage (1985) data are obtained by integrating the portion of energy spectrum in the range of wavelengths 12.5 km $< \lambda_h <$ 25 km, and are reconstructed by summing up the variances in the North–South and East–West directions.

Reference	Method/Source	$\langle\varepsilon\rangle$ ($m^2 s^{-3}$)	U^2 ($m^2 s^{-2}$)
Nastrom and Gage (1985)	Aircraft/GASP (average all flights)	N.A.	0.388
	Aircraft/GASP (average 15–30° N)	N.A.	0.297
	Aircraft/GASP (average 30–45° N)	N.A.	0.426
	Aircraft/GASP (average 45–60° N)	N.A.	0.370
	Aircraft/GASP (average > 60° N)	N.A.	0.234
Lindborg (1999)	Aircraft/MOZAIC (average all flights)	6.0×10^{-5}	N.A.
Lindborg and Cho (2001)	Aircraft/MOZAIC (average 30–40° N)	9.6×10^{-5}	N.A.
	Aircraft/MOZAIC (average 40–50° N)	7.4×10^{-5}	N.A.
	Aircraft/MOZAIC (average 50–60° N)	5.7×10^{-5}	N.A.
	Aircraft/MOZAIC (average 60–70° N)	4.5×10^{-5}	N.A.
Frehlich and Sharman (2010)	Aircraft/AMDAR (average 40–50° N)	5.2×10^{-5}	N.A.
Wroblewski et al. (2010)	Aircraft/Individual flights	1.99×10^{-6}–9.02×10^{-4}	N.A.
Fukao et al. (1994)	Radar/GRATMAC	5×10^{-5}–1×10^{-4}	N.A.
This study	LES (all runs)	8.14×10^{-6}–5.77×10^{-5}	0.215–0.498

ACPD
13, 31891–31932, 2013

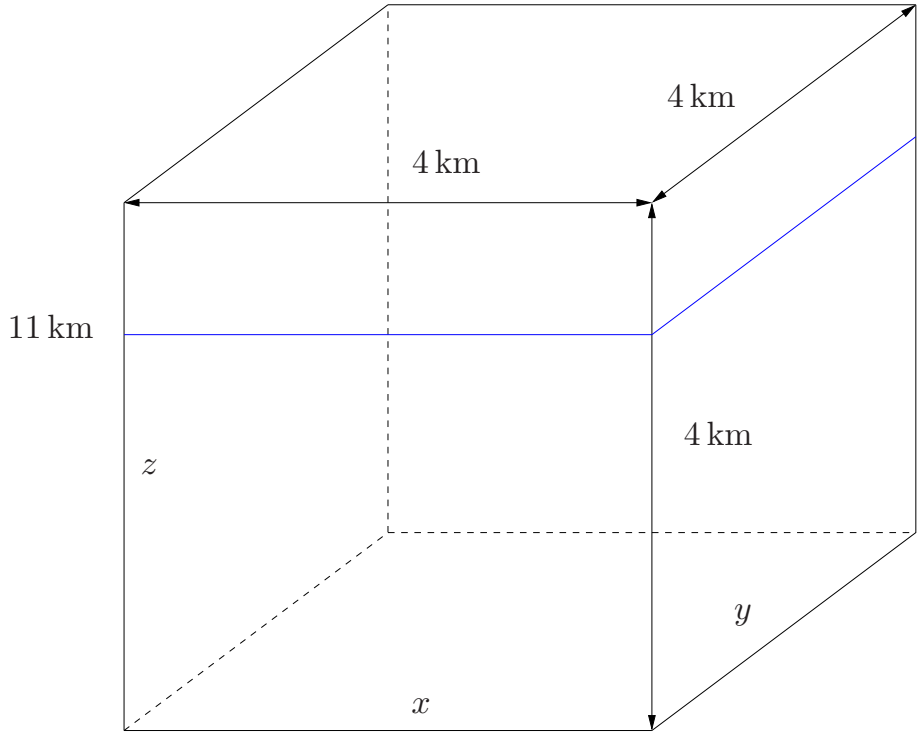

Fig. 1. Sketch of the computational domain.

ACPD
13, 31891–31932, 2013

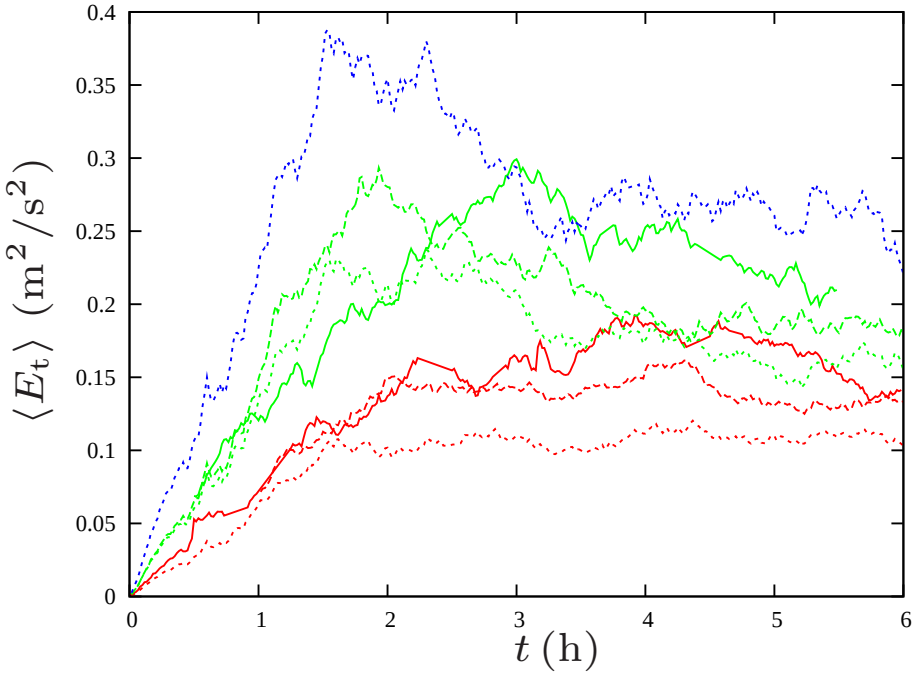

Fig. 2. Temporal evolution of resolved turbulent kinetic energy $\langle E_t \rangle$ for the weak forcing case (red lines), moderate forcing case (green lines), and strong forcing case (blue line). Solid lines: $\Delta = 2$ m; dashed lines: $\Delta = 4$ m; dotted lines: $\Delta = 10$ m.

ACPD
13, 31891–31932, 2013

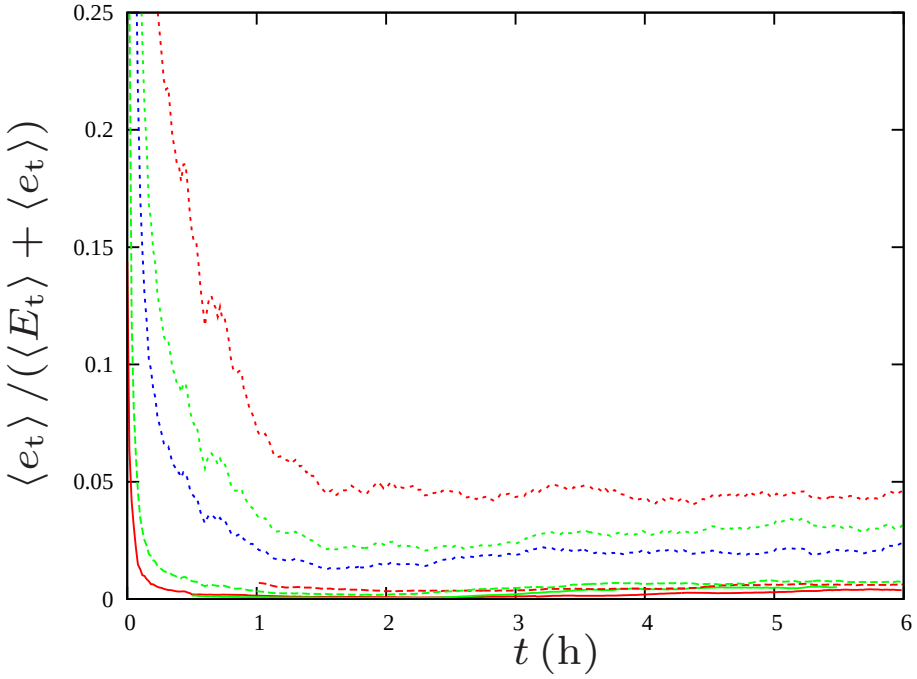

Fig. 3. Temporal evolution of the ratio of subgrid-scale to total turbulent kinetic energy $\mathcal{R} = \langle e_t \rangle / (\langle E_t \rangle + \langle e_t \rangle)$ for weak forcing case (red lines), moderate forcing (green lines) case, and strong forcing case (blue line). Solid lines: $\Delta = 2$ m; dashed lines: $\Delta = 4$ m; dotted lines: $\Delta = 10$ m.

ACPD
13, 31891–31932, 2013

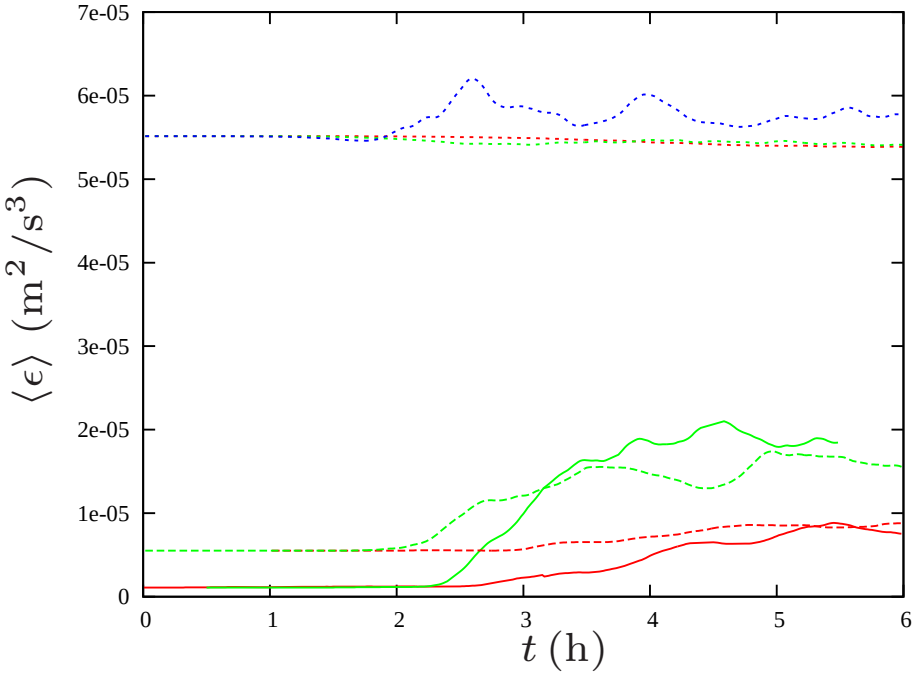

Fig. 4. Temporal evolution of turbulence dissipation rate $\langle \epsilon_t \rangle$ for weak forcing case (red lines), moderate forcing case (green lines), and strong forcing case (blue line). Solid lines: $\Delta = 2$ m; dashed lines: $\Delta = 4$ m; dotted lines: $\Delta = 10$ m.

ACPD
13, 31891–31932, 2013

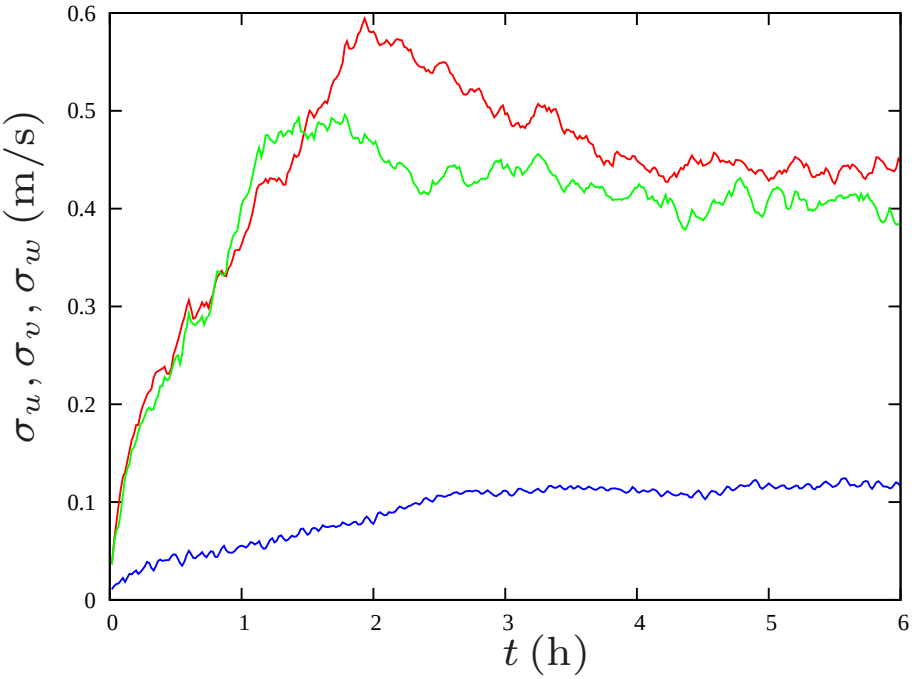

Fig. 5. Temporal evolution of velocity fluctuations σ_u (red lines), σ_v (green lines), and σ_w (blue lines) for the moderate forcing case and $\Delta = 4$ m (run M04).

ACPD
13, 31891–31932, 2013

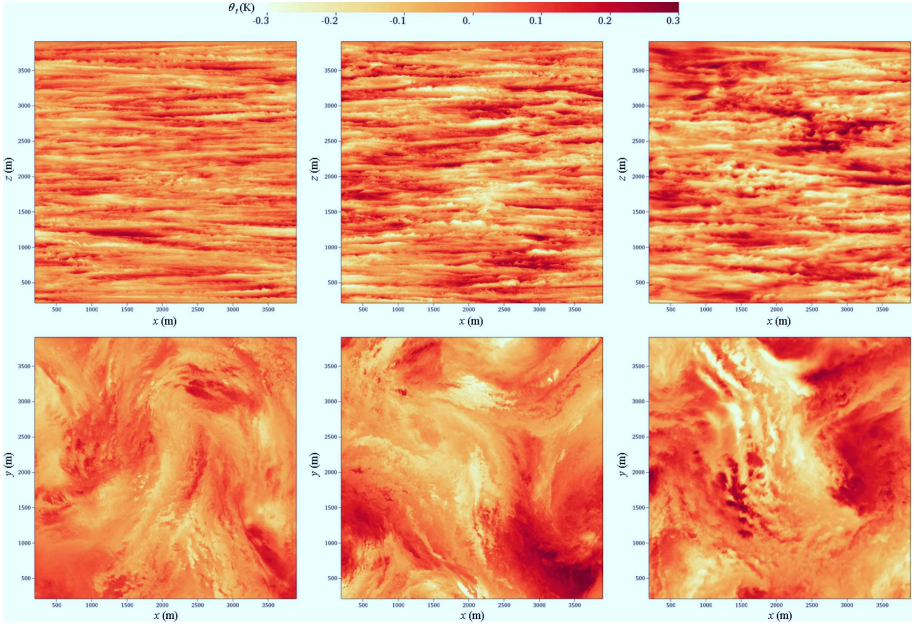

Fig. 6. Snapshots of potential temperature fluctuations θ_t for the weak forcing case, run S02 (left); moderate forcing case, run M02 (center); and strong forcing case, run S10 (right). The top panels show vertical slides taken at $y = L_y/2$, while the bottom panels show horizontal slides taken at $z = L_z/2$.

ACPD
13, 31891–31932, 2013

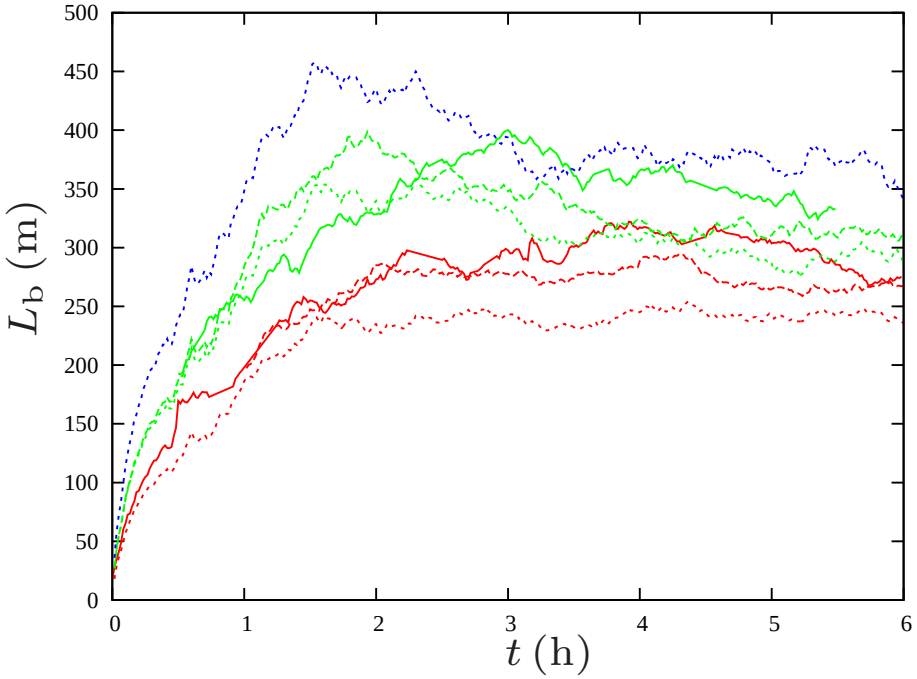

Fig. 7. Temporal evolution of the buoyancy length L_b for the weak forcing cases (red lines), moderate forcing cases (green lines), and strong forcing case (blue line). Solid lines: $\Delta = 2$ m; dashed lines: $\Delta = 4$ m; dotted lines: $\Delta = 10$ m.

ACPD
13, 31891–31932, 2013

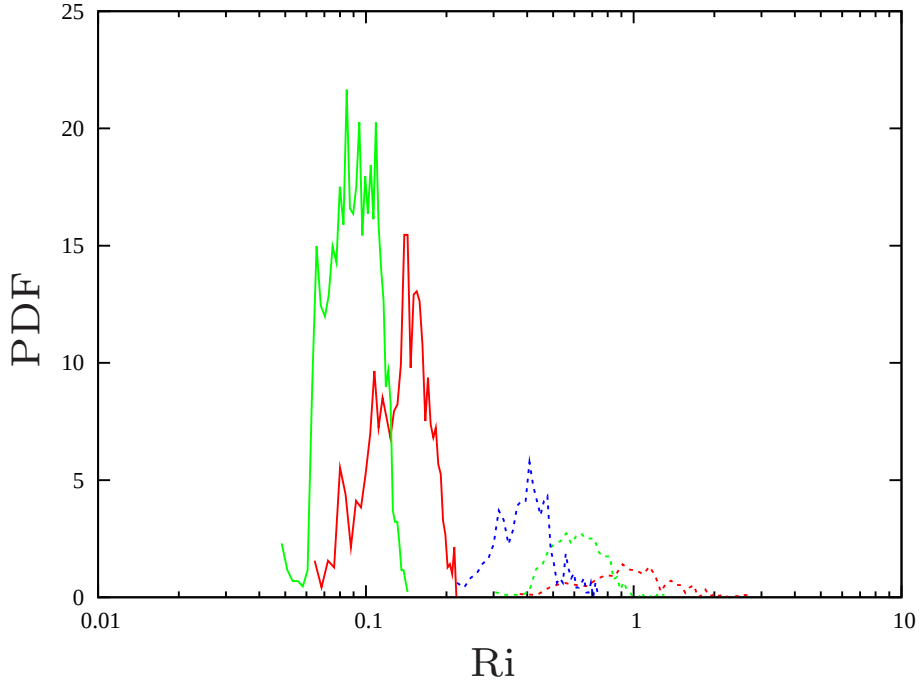

Fig. 8. PDF of Richardson number Ri for the weak forcing cases (red lines); moderate forcing cases (green lines); and strong forcing case (blue line). Solid lines: $\Delta = 2\,\mathrm{m}$; dotted lines: $\Delta = 10\,\mathrm{m}$.

ACPD
13, 31891–31932, 2013

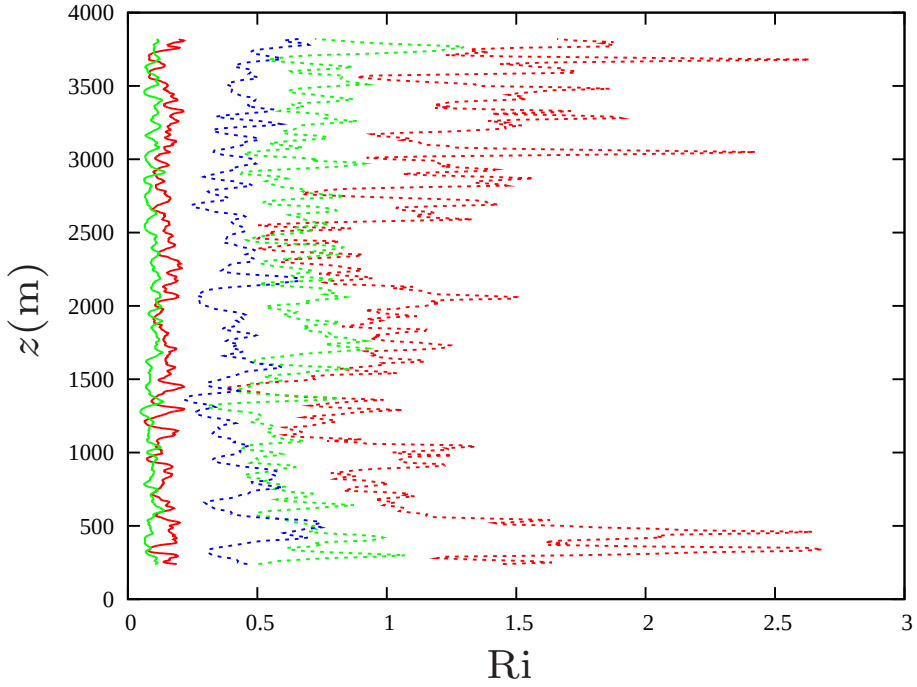

Fig. 9. Vertical distribution of Richardson number Ri for the weak forcing cases (red lines); moderate forcing cases (green lines); and strong forcing case (blue line). Solid lines: $\Delta = 2\,\mathrm{m}$; dotted lines: $\Delta = 10\,\mathrm{m}$.

ACPD
13, 31891–31932, 2013

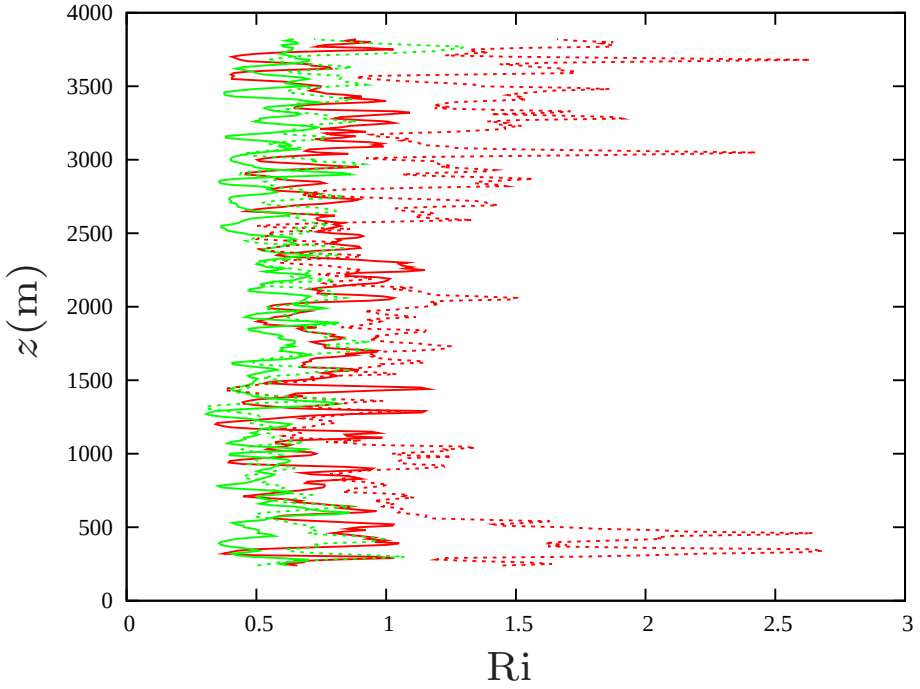

Fig. 10. Effect of filtering on vertical distribution of Richardson number Ri for the weak forcing cases (red lines) and moderate forcing cases (green lines). Solid lines: $\Delta = 2\,\mathrm{m}$ data filtered over $\Delta = 10\,\mathrm{m}$ support; dotted lines: $\Delta = 10\,\mathrm{m}$.

ACPD
13, 31891–31932, 2013

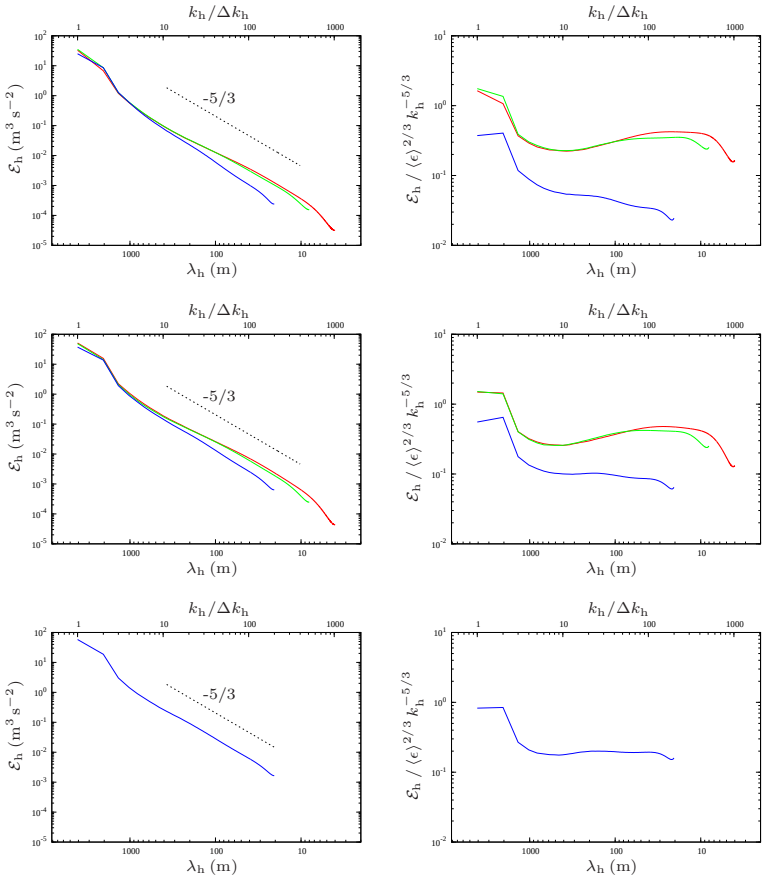

Fig. 11. Horizontal turbulent kinetic energy spectra (left panels) and compensated spectra (right panels). From top to bottom: strong forcing, moderate forcing, and weak forcing case. Red lines: $\Delta = 2\,m$; green lines: $\Delta = 4\,m$; blue lines: $\Delta = 10\,m$.

ACPD
13, 31891–31932, 2013

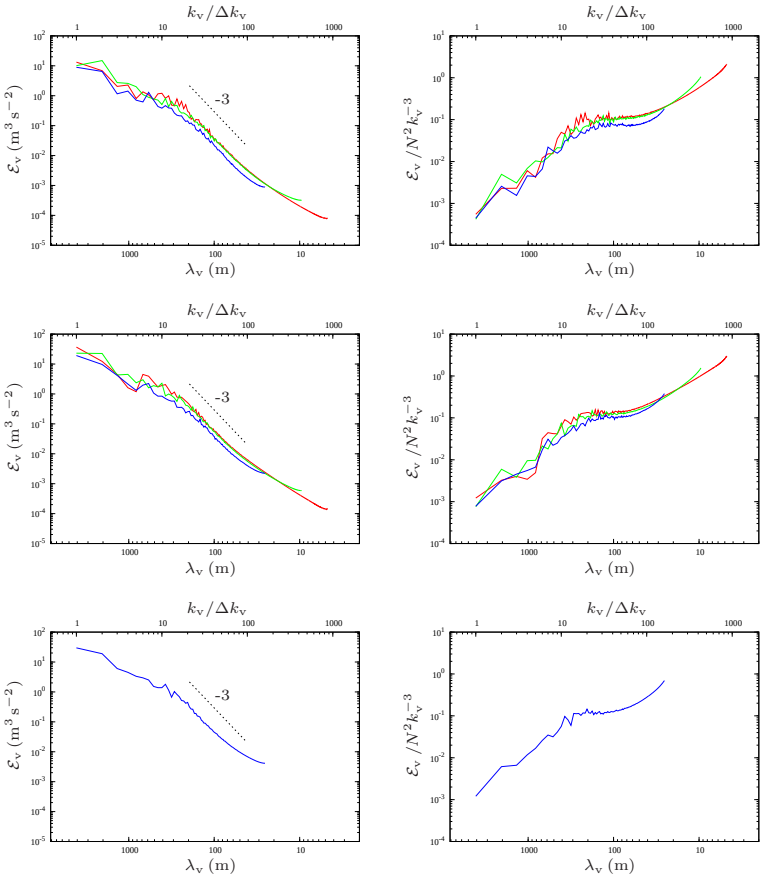

Fig. 12. Vertical turbulent kinetic energy spectra (left panels) and compensated spectra (right panels). From top to bottom: strong forcing, moderate forcing, and weak forcing case. Red lines: $\Delta = 2\,\mathrm{m}$; green lines: $\Delta = 4\,\mathrm{m}$; blue lines: $\Delta = 10\,\mathrm{m}$.

ACPD
13, 31891–31932, 2013